International Journal of Astrophysics and Space Science
2026; 14(1): 1-13
http://www.sciencepublishinggroup.com/j/ijass
doi: 10.11648/j.ijass.20261401.11

Modeling Galactic Oxygen Enrichment via the NOFNe Cycle in Halo and Disk Stars

Swapnajyoti Sarma*, Mrinmay Medhi, Apurba Talukdar, Jinturaj Talukdar, Devapratim Mahanta, Dhanjit Talukdar, Upakul Mahanta, Arup Bharali

Department of Physics, Bhattadev University, Pathsala, India

Email address:

swapnajyoti@gmail.com (Swapnajyoti Sarma), mrinmaymedhi@gmail.com (Mrinmay Medhi), phy.apurba@bhattadevuniversity.ac.in (Apurba Talukdar), jinturajtalukdar@gmail.com (Jinturaj Talukdar), devapratimmahanta@gmail.com (Devapratim Mahanta), phy.dhanjit@bhattadevuniversity.ac.in (Dhanjit Talukdar), phy.upakul@bhattadevuniversity.ac.in (Upakul Mahanta), phy.arup@bhattadevuniversity.ac.in (Arup Bharali)

*Corresponding author

To cite this article:

Swapnajyoti Sarma, Mrinmay Medhi, Apurba Talukdar, Jinturaj Talukdar, Devapratim Mahanta, Dhanjit Talukdar, Upakul Mahanta, Arup Bharali. (2026). Modeling Galactic Oxygen Enrichment via the NOFNe Cycle in Halo and Disk Stars. *International Journal of Astrophysics and Space Science, 14*(1), 1-23. https://doi.org/10.11648/j.ijass.20261401.11

Received: 5 December 2025 ; **Accepted:** 22 December 2025; **Published:** 20 January 2026

Abstract: We present a theoretical analysis of oxygen abundances in a sample of 67 metal-poor field stars belonging to the Galactic halo and disk populations. The primary objective of this study is to investigate whether proton-capture nucleosynthesis pathways can reproduce the observed oxygen abundance trends in metal-poor stellar environments. Oxygen abundances, $[\mathrm{O/H}]_{\mathrm{LTE}}$, are derived under the assumption of local thermodynamic equilibrium. The NOFNe nuclear reaction cycle is modelled under advanced stellar burning conditions, spanning temperatures of 1×10^8–3.5×10^8 K and a characteristic density of $10^2\ \mathrm{g\,cm^{-3}}$. Enhanced stellar atmosphere models and refined abundance calculations yield excellent agreement with reported values, with mean absolute deviations in the range 0.00–0.02 dex. The calculations further reveal subtle but systematic variations in oxygen abundance associated with changes in hydrogen (X_{H}) and oxygen (X_{O}) mass fractions. For the full sample, we obtain a mean oxygen abundance of $\langle[\mathrm{O/H}]\rangle = -0.49$ dex with a mean absolute deviation of 0.19 dex, consistent with expectations for metal-poor stellar populations. Distinct abundance signatures are identified among thick-disk, high-α, and low-α halo stars, reflecting differences in their nucleosynthetic histories and formation pathways. These results provide important constraints on oxygen synthesis in massive stars and supernovae and support a role for proton-capture reactions within the NOFNe cycle, together with rotationally induced mass loss, in shaping the observed surface oxygen abundances. Overall, this study offers new insights into Galactic chemical evolution and the assembly history of the stellar halo.

Keywords: H-burning, Proton-Capture, Metallicity, Nucleosynthesis, NOFNe Cycle

1. Introduction

Globular clusters (GCs) are dense, spherically symmetric stellar systems, typically hosting tens of thousands to millions of stars tightly bound by gravity. These ancient astrophysical laboratories provide critical insights into stellar interiors, nucleosynthetic processes, and galactic chemical evolution [1, 2]. Historically, GC stars were considered coeval, monometallic, ancient, and equidistant, making them ideal for testing stellar evolution models [2]. However, high-resolution spectroscopic surveys have revealed significant chemical heterogeneities among stars, both below and above the main-sequence turnoff, challenging the paradigm of GCs as simple stellar populations (SSPs) [3, 4]. For instance, ω Centauri, the Milky Way's most massive GC, exhibits a pronounced metallicity dispersion, suggesting multiple chemically distinct populations and internal self-enrichment mechanisms [5]. Similar phenomena have been observed in other clusters, such as NGC 2808 and NGC 6752, where photometric and spectroscopic data reveal multiple sequences in color-magnitude diagrams and variations in light element abundances like helium, carbon, nitrogen, oxygen, sodium, and aluminum [6]. Recent reviews emphasize that the multiple population (MP) phenomenon is ubiquitous in Galactic GCs, with stars divided into at least two main groups: a primordial population and one or more enriched populations formed from gas polluted by the ejecta of massive stars from the first generation [8–10]. These findings suggest complex formation scenarios involving multiple episodes of star formation within the clusters, potentially influenced by asymptotic giant branch stars, fast-rotating massive stars, or supermassive stars [11–13].

Elemental abundances in GCs are pivotal for probing stellar dynamics and reconstructing star formation histories. Among these, α-capture elements¯oxygen (O), magnesium (Mg), silicon (Si), calcium (Ca), and titanium (Ti)¯offer key constraints on nucleosynthetic origins and chemical enrichment [14, 15]. Produced primarily in massive stars and dispersed via core-collapse supernovae (Type II SNe), α-elements trace rapid, burst-like star formation episodes [16, 17]. Enhanced [α/Fe] ratios in most Galactic GCs indicate formation in environments dominated by SNe II ejecta before significant iron production from Type Ia supernovae [3, 18]. Oxygen, the third most abundant element after hydrogen and helium, is particularly significant due to its high cosmic abundance and well-characterized synthesis in massive stars, anchoring models of Galactic chemical evolution (GCE) [19, 20]. Its abundance serves as a sensitive probe of internal stellar processes and galactic enrichment drivers. Recent studies have further elucidated the role of α-elements in GCs, with observations of anti-correlations between oxygen and sodium or aluminium in clusters like M13 and NGC 6752, suggesting proton-capture processes in high-temperature environments [21–23]. These chemical signatures are thought to arise from hot bottom burning in intermediate-mass asymptotic giant branch stars or from massive binary interactions, which pollute the intracluster medium with processed material [24, 25]. Additionally, high-precision measurements using facilities like the Very Large Telescope and Gaia have revealed variations in [α/Fe] across different GC populations, providing evidence for diverse enrichment histories and potential accretion of clusters from dwarf galaxies [26, 27].

Early studies laid a robust foundation for oxygen abundance analyses in stellar clusters. Tautvaisiene *et al.* explored α-element enhancements, including oxygen, in red clump stars of open clusters, noting deviations from canonical GCE models [28]. Salaris *et al.* provided theoretical insights into red giant branch evolution, highlighting mixing processes? impact on surface oxygen abundances [29, 34]. Carraro *et al.* contributed observational data on oxygen abundances in intermediate-age clusters, informing evolutionary models [30]. Decressin modelled rapidly rotating massive stars? hydrogen-burning cores to explain abundance anomalies in Galactic GCs [11]. Magrini *et al.* reported near-solar [O/Fe] ratios in clusters like NGC 3960, linked to post-main-sequence surface mixing [32]. Ssmiljanic derived precise [O/H] measurements using the forbidden [OI] 6300 Å line in clusters such as NGC 2324 and NGC 2477, mitigating non-local thermodynamic equilibrium (non-LTE) effects [31]. [33] advanced oxygen abundance determinations through high-resolution spectroscopy. Despite progress, discrepancies between predicted and observed abundances persist due to complexities in α-capture pathways, non-standard mixing, mass loss, and uncertainties in nuclear reaction rates [35, 36].

Building on prior work, such as [37] on proton-capture reactions, this study models oxygen-16 (^{16}O) production via α-capture in the NOFNe chain¯encompassing nitrogen, oxygen, fluorine, and neon¯under helium-enriched conditions typical of late stellar evolutionary phases ($T_9 = 0.1$ to 0.35, density $\sim 10^3$ g/cm^3). The efficiency of related neutron capture processes, such as $^{12}\mathrm{C}(n,\gamma)^{13}\mathrm{C}$, which contributes to the s-process in AGB stars at similar temperatures, further supports the nucleosynthetic framework [38, 39]. By comparing modeled [O/H] values with observed abundances in GC stars, we achieve strong concordance (correlation coefficient of 0.98), underscoring the role of α-capture and neutron capture in modulating surface oxygen levels and advancing our understanding of nucleosynthetic mechanisms and galactic chemical evolution.

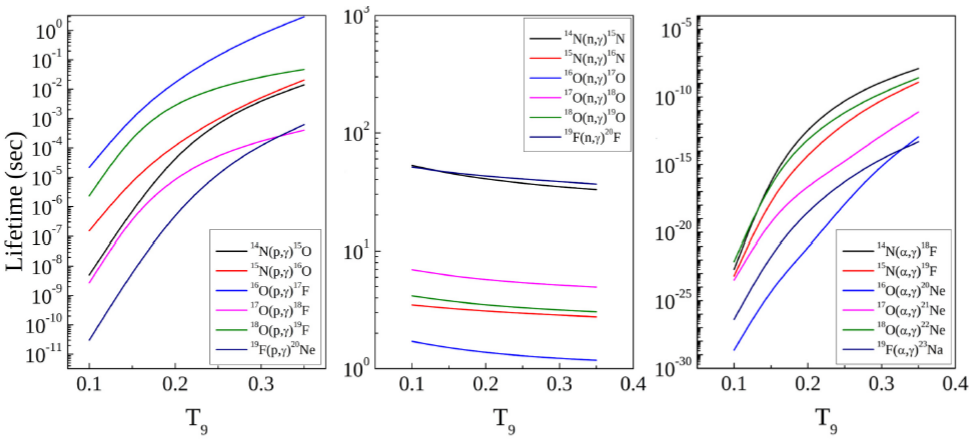

Figure 1. *The plots compare the lifetimes of (p,γ), (α,γ), and (n,γ) reactions for all nuclei involved in the NOFNe nuclear burning cycle.*

This paper is structured as follows: *Section 2* details the theoretical framework, the employed nuclear reaction network, the assumed stellar conditions, and the model for rotational-induced mass ejection. *Section 3* employs the methodology for deriving estimated oxygen abundances, describes the observational data sources for the selected open clusters, and presents a detailed comparison between our model predictions and the observed abundances. Finally, *Section 4* summarises the principal findings and their implications for understanding oxygen nucleosynthesis and stellar chemical enrichment.

2. Theoretical Framework and Nuclear Network

The evolution of stars is governed predominantly by sequential phases of nuclear fusion within their cores. Although temperature serves as the primary determinant in these stellar mechanisms, density exerts an influence as well, albeit one that is generally subordinate due to its linear impact on reaction rates, despite spanning multiple orders of magnitude. Consequently, density plays a minimal role in nucleosynthesis, except under regimes characterised by low temperatures and elevated densities. Within the conventional stellar paradigm, stars are modeled as spherically symmetric entities, absent magnetic fields, rotation, or surface mass ejection. Under such simplifications, nucleosynthetic products generated in proximity to the core are conveyed to the stellar surface via convective processes, which constitute the principal mechanism for material mixing. Convective regions are assumed to exhibit complete homogenization [40]

In advanced evolutionary stages, dredge-up phenomena markedly alter surface elemental compositions. Nonetheless, in red giant branch (RGB) stars, standard extra-mixing processes do not modify surface abundances unless amplified. Potential triggers for this amplification include tidal acceleration in close binary systems during the upper RGB phase [41], or intrinsic stellar dynamics in isolated stars that intensify mixing near the RGB tip. In the latter case, enhanced mixing may penetrate the hydrogen-burning shell, initiating supplementary nuclear reactions that facilitate the synthesis of primary isotopes such as ^{14}N, ^{13}C, ^{16}O, and ^{12}C. The aggregate abundance of carbon, nitrogen, and oxygen (C + N + O) maintains near-constancy in stellar environments [42], contributing to the observed levels of ^{19}F. The production of ^{12}C arises from incomplete helium fusion within the helium-enriched intershell [43]. Furthermore, the incorporation of protons¯termed partial mixing [44]¯into the helium-rich intershell is essential for s-process activation in these objects [45]. This analysis, however, refrains from exploring the underlying physical drivers of mixing and dredge-up.

Considering the above physical aspects, we assumed a stellar situation in which, at high temperature and low density, the reaction $^{12}C(n,\gamma)^{13}C$ may occur in stars as part of nucleosynthesis Käppeler et al. (2011) [38] and Iliadis (2007) [39], where a ^{12}C nucleus captures a neutron and emits a γ photon, forming ^{13}C. At $T_9 = 0.1$ K, the thermal energy of free neutrons follows a Maxwell-Boltzmann distribution, with an average kinetic energy given by:

$$E_k \approx \frac{3}{2} k_B T \approx 8.6 \times 10^{-3}\ \text{MeV} \times 100 \approx 0.86\ \text{MeV}$$

At a temperature of approximately 0.3 GK, the α-capture reaction on ^{14}N proceeds with significant efficiency. In stellar interiors, the requisite α-particle flux is primarily supplied during helium-burning episodes or through thermal pulses in advanced evolutionary phases. This reaction is of particular relevance in asymptotic giant branch (AGB) stars, where fluorine nucleosynthesis occurs under conditions of high nitrogen abundance produced by preceding CNO-cycle activity. The isotope ^{14}N, which constitutes 99.63% of terrestrial nitrogen [46], thus serves as the principal seed nucleus for this pathway. The resulting ^{18}F is unstable and may undergo subsequent proton-capture reactions, thereby contributing to the synthesis of ^{19}F and providing a potential link to the production of neon isotopes.

Table 1. *Table for Branching Ratio.*

T_9	$B_r(^{16}\text{O})$
0.10	6.32×10^{-20}
0.15	3.58×10^{-17}
0.20	2.16×10^{-15}
0.25	6.55×10^{-13}
0.30	1.15×10^{-10}
0.35	4.21×10^{-09}

Table 2. *The table presents reaction rates and lifetimes for (p,γ) nuclear reactions at density $\rho = 10^2$ gm/cc. T_9 is the temperature in units of 10^9 K, $N_A < \sigma\nu >$ is the reaction rate parameter, and τ_r is the reaction lifetime in sec. .*

Reaction	T_9	$N_A < \sigma\nu >$	τ_r
$^{14}N(p,\gamma)^{15}O$	0.10	$7.20 \times 10^{+1}$	7.98×10^{-7}
	0.15	1.14×10^{-4}	7.98×10^{-7}
	0.20	2.50×10^{-4}	5.50×10^{-5}
	0.25	1.09×10^{-1}	7.63×10^{-4}
	0.30	2.00×10^{-1}	4.24×10^{-3}
	0.35	$6.00 \times 10^{+0}$	1.40×10^{-2}
$^{15}N(p,\gamma)^{16}O$	0.10	2.16×10^{-5}	1.51×10^{-7}
	0.15	1.24×10^{-3}	8.68×10^{-6}
	0.20	1.88×10^{-2}	1.32×10^{-4}
	0.25	1.48×10^{-1}	1.04×10^{-3}
	0.30	7.72×10^{-1}	5.40×10^{-3}
	0.35	$2.95 \times 10^{+0}$	2.07×10^{-2}
$^{16}O(p,\gamma)^{17}F$	0.10	1.26×10^{-7}	8.82×10^{-10}
	0.15	8.48×10^{-6}	5.94×10^{-8}
	0.20	1.18×10^{-4}	8.26×10^{-7}
	0.25	7.57×10^{-4}	5.30×10^{-6}
	0.30	3.09×10^{-3}	2.16×10^{-5}
	0.35	9.44×10^{-3}	6.61×10^{-5}
$^{17}O(p,\gamma)^{18}F$	0.10	3.89×10^{-7}	2.72×10^{-9}
	0.15	7.41×10^{-5}	5.19×10^{-7}

Reaction	T_9	$N_A < \sigma\nu >$	τ_r
	0.20	1.46×10^{-3}	1.02×10^{-5}
	0.25	8.24×10^{-3}	5.77×10^{-5}
	0.30	2.52×10^{-2}	1.76×10^{-4}
	0.35	5.78×10^{-2}	4.05×10^{-4}
$^{18}O(p,\gamma)^{19}F$	0.10	3.32×10^{-4}	2.32×10^{-6}
	0.15	4.40×10^{-2}	3.08×10^{-4}
	0.20	4.87×10^{-1}	3.41×10^{-3}
	0.25	$1.68 \times 10^{+0}$	1.18×10^{-2}
	0.30	$3.85 \times 10^{+0}$	2.70×10^{-2}
	0.35	$6.74 \times 10^{+0}$	4.72×10^{-2}
$^{19}F(p,\gamma)^{20}Ne$	0.10	4.31×10^{-9}	3.02×10^{-11}
	0.15	9.55×10^{-7}	6.69×10^{-9}
	0.20	8.67×10^{-5}	6.07×10^{-7}
	0.25	2.14×10^{-3}	1.50×10^{-5}
	0.30	1.89×10^{-2}	1.32×10^{-4}
	0.35	8.86×10^{-2}	6.20×10^{-4}

Table 3. *The table presents reaction rates and lifetimes for (p,γ) nuclear reactions at density $\rho = 10^2$ gm/cc. T_9 is the temperature in units of 10^9 K, $N_A < \sigma\nu >$ is the reaction rate parameter, and τ_r is the reaction lifetime in sec.*

Reaction	T_9	$N_A < \sigma\nu >$	τ_r
$^{14}N(p,\gamma)^{15}O$	0.10	$7.20 \times 10^{+1}$	7.98×10^{-7}
	0.15	1.14×10^{-4}	7.98×10^{-7}
	0.20	2.50×10^{-4}	5.50×10^{-5}
	0.25	1.09×10^{-1}	7.63×10^{-4}
	0.30	2.00×10^{-1}	4.24×10^{-3}
	0.35	$6.00 \times 10^{+0}$	1.40×10^{-2}
$^{15}N(p,\gamma)^{16}O$	0.10	2.16×10^{-5}	1.51×10^{-7}
	0.15	1.24×10^{-3}	8.68×10^{-6}
	0.20	1.88×10^{-2}	1.32×10^{-4}
	0.25	1.48×10^{-1}	1.04×10^{-3}
	0.30	7.72×10^{-1}	5.40×10^{-3}
	0.35	$2.95 \times 10^{+0}$	2.07×10^{-2}
$^{16}O(p,\gamma)^{17}F$	0.10	1.26×10^{-7}	8.82×10^{-10}
	0.15	8.48×10^{-6}	5.94×10^{-8}
	0.20	1.18×10^{-4}	8.26×10^{-7}
	0.25	7.57×10^{-4}	5.30×10^{-6}
	0.30	3.09×10^{-3}	2.16×10^{-5}
	0.35	9.44×10^{-3}	6.61×10^{-5}
$^{17}O(p,\gamma)^{18}F$	0.10	3.89×10^{-7}	2.72×10^{-9}
	0.15	7.41×10^{-5}	5.19×10^{-7}
	0.20	1.46×10^{-3}	1.02×10^{-5}
	0.25	8.24×10^{-3}	5.77×10^{-5}
	0.30	2.52×10^{-2}	1.76×10^{-4}
	0.35	5.78×10^{-2}	4.05×10^{-4}
$^{18}O(p,\gamma)^{19}F$	0.10	3.32×10^{-4}	2.32×10^{-6}
	0.15	4.40×10^{-2}	3.08×10^{-4}
	0.20	4.87×10^{-1}	3.41×10^{-3}
	0.25	$1.68 \times 10^{+0}$	1.18×10^{-2}
	0.30	$3.85 \times 10^{+0}$	2.70×10^{-2}
	0.35	$6.74 \times 10^{+0}$	4.72×10^{-2}
$^{19}F(p,\gamma)^{20}Ne$	0.10	4.31×10^{-9}	3.02×10^{-11}
	0.15	9.55×10^{-7}	6.69×10^{-9}
	0.20	8.67×10^{-5}	6.07×10^{-7}

Reaction	T_9	$N_A < \sigma\nu >$	τ_r
	0.25	2.14×10^{-3}	1.50×10^{-5}
	0.30	1.89×10^{-2}	1.32×10^{-4}
	0.35	8.86×10^{-2}	6.20×10^{-4}

Table 4. *The table presents reaction rates and lifetimes for (n,γ) nuclear reactions at density $\rho = 10^2$ gm/cc. T_9 is the temperature in units of 10^9 K, $N_A < \sigma\nu >$ is the reaction rate parameter, and τ_r is the reaction lifetime in sec .*

Reaction	T_9	$N_A < \sigma\nu >$	τ_r
$^{14}N(n,\gamma)^{15}N$	0.10	$2.26 \times 10^{+5}$	$5.27 \times 10^{+1}$
	0.15	$2.26 \times 10^{+5}$	$4.51 \times 10^{+1}$
	0.20	$2.02 \times 10^{+5}$	$4.04 \times 10^{+1}$
	0.25	$1.86 \times 10^{+5}$	$3.72 \times 10^{+1}$
	0.30	$1.74 \times 10^{+5}$	$3.47 \times 10^{+1}$
	0.35	$1.64 \times 10^{+5}$	$3.29 \times 10^{+1}$
$^{15}N(n,\gamma)^{16}N$	0.10	$1.74 \times 10^{+4}$	$3.49 \times 10^{+0}$
	0.15	$1.63 \times 10^{+4}$	$3.26 \times 10^{+0}$
	0.20	$1.55 \times 10^{+4}$	$3.09 \times 10^{+0}$
	0.25	$1.48 \times 10^{+4}$	$2.96 \times 10^{+0}$
	0.30	$1.43 \times 10^{+4}$	$2.85 \times 10^{+0}$
	0.35	$1.38 \times 10^{+4}$	$2.76 \times 10^{+0}$
$^{16}O(n,\gamma)^{17}O$	0.10	$8.53 \times 10^{+3}$	$1.71 \times 10^{+0}$
	0.15	$7.49 \times 10^{+3}$	$1.50 \times 10^{+0}$
	0.20	$6.85 \times 10^{+3}$	$1.37 \times 10^{+0}$
	0.25	$6.42 \times 10^{+3}$	$1.28 \times 10^{+0}$
	0.30	$6.10 \times 10^{+3}$	$1.22 \times 10^{+0}$
	0.35	$5.89 \times 10^{+3}$	$1.18 \times 10^{+0}$
$^{17}O(n,\gamma)^{18}O$	0.10	$3.47 \times 10^{+4}$	$6.95 \times 10^{+0}$
	0.15	$3.10 \times 10^{+4}$	$6.19 \times 10^{+0}$
	0.20	$2.86 \times 10^{+4}$	$5.72 \times 10^{+0}$
	0.25	$2.69 \times 10^{+4}$	$5.39 \times 10^{+0}$
	0.30	$2.57 \times 10^{+4}$	$5.13 \times 10^{+0}$
	0.35	$2.47 \times 10^{+4}$	$4.94 \times 10^{+0}$
$^{18}O(n,\gamma)^{19}O$	0.10	$2.08 \times 10^{+4}$	$4.17 \times 10^{+0}$
	0.15	$1.88 \times 10^{+4}$	$3.76 \times 10^{+0}$
	0.20	$1.75 \times 10^{+4}$	$3.49 \times 10^{+0}$
	0.25	$1.65 \times 10^{+4}$	$3.30 \times 10^{+0}$
	0.30	$1.58 \times 10^{+4}$	$3.15 \times 10^{+0}$
	0.35	$1.52 \times 10^{+4}$	$3.05 \times 10^{+0}$
$^{19}F(n,\gamma)^{20}F$	0.10	$2.55 \times 10^{+5}$	$5.11 \times 10^{+1}$
	0.15	$2.30 \times 10^{+5}$	$4.61 \times 10^{+1}$
	0.20	$2.14 \times 10^{+5}$	$4.28 \times 10^{+1}$
	0.25	$2.02 \times 10^{+5}$	$4.04 \times 10^{+1}$
	0.30	$1.92 \times 10^{+5}$	$3.84 \times 10^{+1}$
	0.35	$1.83 \times 10^{+5}$	$3.66 \times 10^{+1}$

Table 5. *The table presents reaction rates and lifetimes for (α,γ) nuclear reactions for density $\rho = 10^2$ gm/cc. T_9 is the temperature in units of 10^9 K, $N_A < \sigma\nu >$ is the reaction rate parameter, and τ_r is the reaction lifetime in sec .*

Reaction	T_9	$N_A < \sigma\nu >$	τ_r
$^{14}N(\alpha,\gamma)^{18}F$	0.10	3.71×10^{-21}	2.06×10^{-23}
	0.15	7.18×10^{-14}	2.01×10^{-16}
	0.20	2.09×10^{-10}	5.85×10^{-13}
	0.25	2.32×10^{-08}	6.50×10^{-11}

Reaction	T_9	$N_A < \sigma\nu >$	τ_r
	0.30	5.10×10^{-07}	1.43×10^{-09}
	0.35	4.47×10^{-06}	1.25×10^{-08}
$^{15}N(\alpha,\gamma)^{19}F$	0.10	2.41×10^{-21}	6.75×10^{-24}
	0.15	1.71×10^{-15}	4.79×10^{-18}
	0.20	2.22×10^{-12}	6.22×10^{-15}
	0.25	4.47×10^{-10}	1.25×10^{-12}
	0.30	2.29×10^{-08}	6.41×10^{-11}
	0.35	4.36×10^{-07}	1.22×10^{-09}
$^{16}O(\alpha,\gamma)^{20}Ne$	0.10	7.96×10^{-27}	2.23×10^{-29}
	0.15	3.04×10^{-22}	8.51×10^{-25}
	0.20	2.55×10^{-19}	7.14×10^{-22}
	0.25	4.96×10^{-16}	1.39×10^{-18}
	0.30	3.56×10^{-13}	9.97×10^{-16}
	0.35	3.97×10^{-11}	1.11×10^{-13}
$^{17}O(\alpha,\gamma)^{21}Ne$	0.10	1.20×10^{-21}	3.36×10^{-24}
	0.15	4.38×10^{-17}	1.23×10^{-19}
	0.20	1.02×10^{-14}	2.86×10^{-17}
	0.25	5.84×10^{-13}	1.64×10^{-15}
	0.30	5.53×10^{-11}	1.55×10^{-13}
	0.35	2.70×10^{-09}	7.56×10^{-12}
$^{18}O(\alpha,\gamma)^{22}Ne$	0.10	2.73×10^{-20}	7.64×10^{-23}
	0.15	3.29×10^{-14}	9.21×10^{-17}
	0.20	3.79×10^{-11}	1.06×10^{-13}
	0.25	2.95×10^{-09}	8.26×10^{-12}
	0.30	7.33×10^{-08}	2.05×10^{-10}
	0.35	9.38×10^{-07}	2.63×10^{-09}
$^{19}F(\alpha,\gamma)^{23}Na$	0.10	1.49×10^{-24}	4.17×10^{-27}
	0.15	1.24×10^{-19}	3.48×10^{-22}
	0.20	2.52×10^{-16}	6.50×10^{-19}
	0.25	2.32×10^{-14}	4.25×10^{-17}
	0.30	1.06×10^{-12}	2.98×10^{-15}
	0.35	1.71×10^{-11}	4.80×10^{-14}

1. $^{14}N(\alpha,\gamma)^{18}F$: This reaction is relevant at $0.2 \leq T_9 \leq 0.4$, characteristic of helium flashes and intershell burning in AGB stars. Its rate is dominated by low-energy resonances at $E_{\rm cm} = 470$ and 566 keV [47], with higher-energy contributions negligible. Rates and uncertainties are adopted from Iliadis *et al.* (2010) [48], with errors $\sim 10\%$ over $T_9 = 0.1˘1.0$.
2. ^{18}F, being β^+ unstable, decays to ^{18}O much faster than proton capture in the considered stellar conditions, enabling subsequent ^{18}O processing via proton-induced alpha emission.
3. $^{18}O(p,\alpha)^{15}N$: Influences the production of ^{15}N, ^{18}O, and ^{19}F, tracers of nucleosynthesis and mixing in AGB stars. Low-background measurements at LUNA reach $E_{\rm cm} = 55$ keV with $\sigma < 1$ pb/sr [49]. Reaction rates follow NACRE II [50].
4. $^{15}N(\alpha,\gamma)^{19}F$: Resonant at astrophysical energies, with recent measurements increasing the rate by $\sim 15\%$ at $T_9 < 0.1$ [51]. Adopted rates are from Iliadis *et al.* (2010) [48], with uncertainties $\sim 15\%$.
5. $^{19}F(p,\alpha)^{16}O$: A primary destruction channel for fluorine. Monte Carlo evaluations yield rates up to twice the NACRE value at low T_9 [52]. For this work, Iliadis *et al.* (2010) rates are used, with $\sim 20\%$ uncertainties.
6. $^{16}O(p,\gamma)^{17}F$: Relevant at $0.06 \leq T_9 \leq 0.1$ for hot bottom burning in AGB stars. Resonances at $E_{\rm cm} = 2.50$ and 3.26 MeV [53] are negligible. Rates from Iliadis *et al.* (2010) carry $\sim 7\%$ uncertainty.
7. ^{17}F, β^+ unstable, decays to ^{17}O faster than proton capture, leading to branching between (α,n) and (α,γ) paths. Branching ratios indicate (α,n) dominates, forming ^{20}Ne and recycling neutrons [47].
8. $^{17}O(\alpha,n)^{20}Ne$: Reaction rates are sensitive to uncertainties in ^{21}Ne excited states, favoring neutron recycling [54]. Adopted rates from Iliadis *et al.* (2010) carry $\sim 25\%$ uncertainty.
9. $^{16}O(\alpha,\gamma)^{20}Ne$: Cross-section at low energies includes direct capture and resonances. Recent evaluations suggest rates up to twice older compilations below $T_9 = 0.2$ [55]. Iliadis *et al.* (2010) rates are used.

For the present work, we use the reaction rate determination by NACRE II [50]. In this study, we compared the reaction rates from the NACRE compilation [56] and recent evaluations [57] to examine the extent of ^{16}O abundance variation. Thus, the NOFNe cycle (Figure 2) is as follows:

$$\begin{aligned}
{}^{14}_{7}N + {}^{4}_{2}He &\rightarrow {}^{18}_{9}F + \gamma \\
{}^{18}_{9}F &\rightarrow {}^{18}_{8}O + {}^{0}_{+1}e + \nu_e \\
{}^{18}_{8}O + {}^{1}_{1}H &\rightarrow {}^{19}_{9}F + \gamma \\
{}^{19}_{9}F + {}^{1}_{1}H &\rightarrow {}^{16}_{8}O + {}^{4}_{2}He \\
{}^{16}_{8}O + {}^{4}_{2}He &\rightarrow {}^{20}_{10}Ne + \gamma \\
{}^{16}_{8}O + {}^{1}_{1}H &\rightarrow {}^{17}_{9}F + \gamma \\
{}^{17}_{9}F &\rightarrow {}^{17}_{8}O + {}^{0}_{+1}e + \nu_e \\
{}^{17}_{8}O + {}^{4}_{2}He &\rightarrow {}^{20}_{10}Ne + {}^{1}_{0}n \\
{}^{16}_{8}O + {}^{4}_{2}He &\rightarrow {}^{20}_{10}Ne + \gamma
\end{aligned} \tag{1}$$

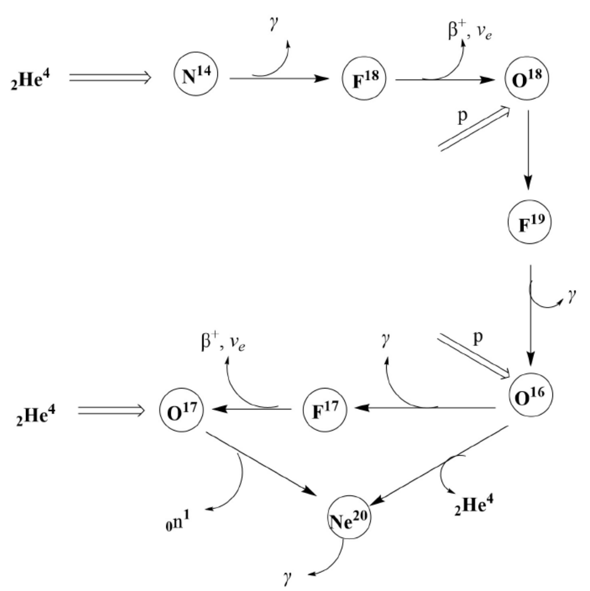

Figure 2. *The NOFNe nuclear burning cycle.*

3. Reaction Network and Formalism

The reaction cycle under consideration produces, in each full loop (independent of branching), a single α-particle together with two electron neutrinos (ν_e) and two positrons (e^+). The progenitor nuclei primarily act as catalysts, such that the total nuclear mass and number are conserved across the cycle, while hydrogen and helium are gradually depleted. The net outcome of the reaction sequence can therefore be summarized as:

$$\frac{dN_H}{dt} < 0, \quad \frac{dN_{He}}{dt} < 0. \tag{2}$$

The general time evolution of the number density of a nucleus subject to proton capture or β-decay, in the absence of branching, is given by Clayton [60]:

$$\dot{N}i = -N_i N_p \langle \sigma v \rangle p, i + N_j N_p \langle \sigma v \rangle_{p,j} \pm \lambda_k N_k, \tag{3}$$

where $\langle \sigma v \rangle_{p,i}$ represents the thermally averaged proton-capture rate on species i, and λ_k is the decay constant of an unstable isotope k.

Since the cycle involves both proton captures and β-decays, the relative timescales of these processes control the flow of abundances. When the β-decay lifetime (τ_β) of an unstable nucleus is much shorter than its proton capture lifetime (τ_p), the β-decay can be treated as instantaneous. In this limit, the decay can be absorbed into the reaction chain, yielding an effective process of the form:

$$A_i Y(p, \gamma e^+ \nu_e) A_{i+1} Y, \tag{4}$$

where Y denotes any stable nucleus and A_i is the mass number of the isotope.

In terms of mass fractions, the corresponding rate equation becomes:

$$\dot{X}i = \left(-Rp, i X_i X_p \rho + \frac{A_i}{A_j} R_{p,j} X_j X_p \rho \right), \tag{5}$$

where $R_p = N_A \langle \sigma v \rangle$ is the rate parameter, and A_i, A_j denote the mass numbers of the nuclei involved. Reformulating Eq. (4) relative to the hydrogen mass fraction, the system reduces to a set of coupled first-order linear differential equations for each cycle:

$$\frac{dX_i}{dX_p} = \left(-R_{p,i} X_i + \frac{A_i}{A_j} R_{p,j} X_j \right) \left(-\frac{A_j}{A_i} \frac{1}{A_i} R_{p,i} X_i \right)^{-1}. \tag{6}$$

This formulation provides a consistent framework for describing hydrogen depletion and the evolution of elemental abundances within the cycle.

4. Neutron Production and Capture

The cycle also produces free neutrons, which in principle could participate in (n, γ) or (n, p) reactions, thereby opening additional branching points in the network. The neutron-capture lifetime of a nucleus is expressed as:

$$\tau_n = \frac{1}{N_A \langle \sigma v \rangle X_n \rho}. \tag{7}$$

Neutron-capture lifetimes for all stable isotopes were calculated analogously to proton captures, using NACRE II compilation rates for the relevant reactions. Potential (n, p) channels such as $^{18}O(n,p)^{18}N$ and $^{19}F(n,p)^{19}O$ were also examined. However, these processes are negligible, as their capture lifetimes remain much larger than evolutionary timescales, even at $T_9 = 0.3$.

Moreover, the computed neutron-capture lifetimes exceed the typical ages of globular clusters ($\sim 10^{10}$ yr; e.g., 12.0 Gyr for 47 Tuc and 12.6 $\pm$ 0.7 Gyr for NGC 6397 [59]). Consequently, neutron-capture reactions can be safely excluded from the reaction network over the considered temperature range.

Figure 1 presents a comparative overview of the α-capture and neutron-capture lifetimes for the nuclei participating in the cycle, illustrating the dominance of α-induced processes in governing the overall reaction flow.

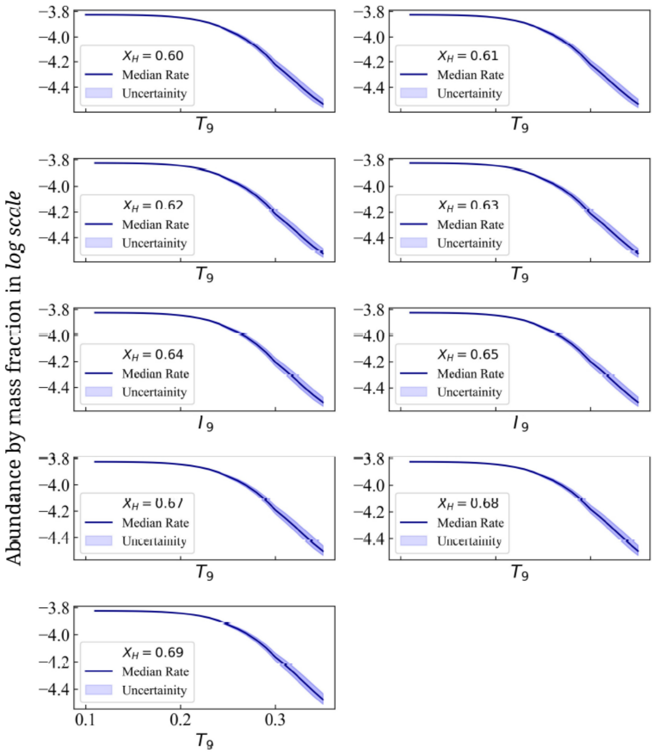

Figure 3. *The estimated abundance by mass fraction of* ^{16}O *is plotted as functions of temperature* T_9 *for different hydrogen mass fractions* (X_H) *for the initial condition* $X_{he} = 0.0010$, *across a temperature range of* T_9 *from 0.10 to 0.35 K.*

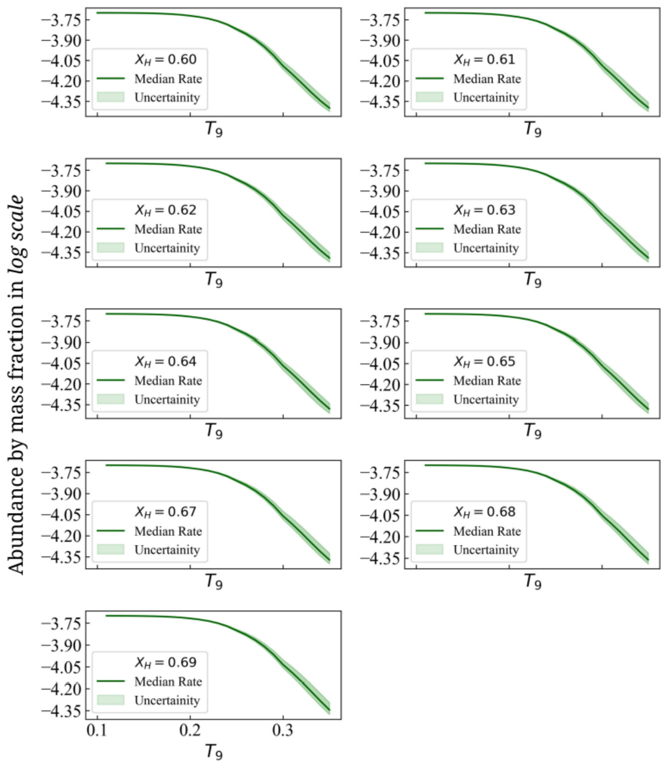

Figure 4. The estimated abundance by mass fraction of ^{16}O is plotted as functions of temperature T_9 for different hydrogen mass fractions (X_H) for initial condition $X_{he} = 0.0015$, across a temperature range of T_9 from 0.10 to 0.35 K.

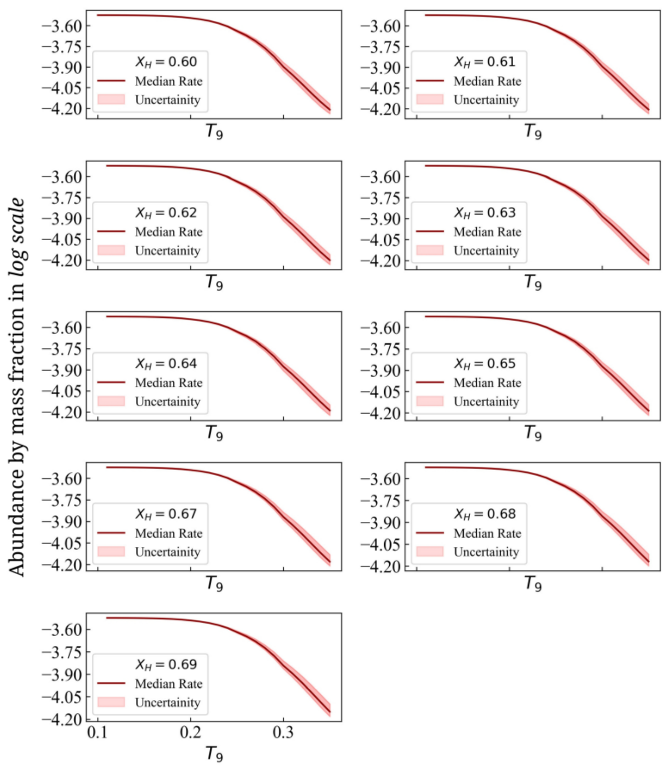

Figure 5. The estimated abundance by mass fraction of ^{16}O is plotted as functions of temperature T_9 for different hydrogen mass fractions (X_H) for initial condition $X_{he} = 0.0020$, across a temperature range of T_9 from 0.10 to 0.35 K.

4.1. Numerical Determination of ^{16}O Abundance in the Reaction Network

In this study, the temporal evolution of elemental abundances in the NOFNe cycle is described through a system of nine coupled, first-order linear differential equations. These equations are expressed in terms of mass fractions and solved numerically using computational software. The hydrogen mass fraction is fixed at $X_H = 0.60$ in order to determine the equilibrium mass fraction of ^{16}O under varying initial heavy-element compositions. The adopted primordial composition follows the standard distribution:

$$X_H = 0.70, \quad X_{He} = 0.28, \quad \text{and} \quad X_{he} = 0.02,$$

ensuring compliance with the normalisation condition:

$$X_H + X_{He} + X_{he} = 1. \tag{8}$$

The heavy element mass fraction is systematically varied as follows: $X_{he} = (X_{^{14}N} = X_{^{15}N} = X_{^{16}O} = X_{^{17}O} = X_{^{18}O} = X_{^{19}F} = X_{^{20}Ne} = 0.00015) = 0.0010$, $X_{he} = (X_{^{14}N} = X_{^{15}N} = X_{^{16}O} = X_{^{17}O} = X_{^{18}O} = X_{^{19}F} = X_{^{20}Ne} = 0.00020) = 0.0015$, and $X_{he} = (X_{^{14}N} = X_{^{15}N} = X_{^{16}O} = X_{^{17}O} = X_{^{18}O} = X_{^{19}F} = X_{^{20}Ne} = 0.00030) = 0.0020$, while maintaining a constant X_H. The equilibrium abundance of ^{16}O, expressed as a mass fraction, is computed for each set of initial conditions. The results are presented in Figures 3 ˘ 5. Across all cases, hydrogen depletion directly impacts the relative enhancement or depletion of heavier isotopes. At $T_9 \leq 0.30$, the ^{16}O mass fraction decreases with increasing temperature, reflecting enhanced competition from α- and proton-capture channels. The maximum deviation in equilibrium abundance, relative to the initial configuration, remains below 8% for metallicities of order $Z \sim 5 \times 10^{-4}$. For $T_9 \geq 0.30$, the ^{16}O abundance approaches a stable equilibrium value, showing negligible variation across different initial metallicities. In particular, for the lowest metallicity case ($Z \sim 10^{-4}$), the ^{16}O abundance remains essentially unchanged within the adopted uncertainty range.

These results highlight the sensitivity of ^{16}O abundance to temperature in the regime $T_9 \leq 0.30$, while demonstrating stability at higher temperatures. The metallicity dependence is weak, consistent with the catalytic nature of the cycle. Furthermore, the comparison of NACRE and Iliadis rates shows that the uncertainty in ^{16}O mass fraction remains within $\sim 10\%$ across the relevant stellar temperature range. Thus, the NOFNe cycle preserves ^{16}O abundance under typical stellar conditions, with only mild variations arising from temperature-induced changes in competing reaction channels.

Table 6. *The elemental abundance for ^{16}O are found at different hydrogen mass fractions. All observational data (T_{eff}, log g, [Fe/H], and $[O/H]^a_{LTE}$) are from [61].*

Star	T_{eff} (K)	Log g	[Fe/H]	$[O/H]^a_{LTE}$	$[O/H]^o$	T_9^o	X_H^o	X_O^o	δ	MAD
BD-21 3420	5808	4.26	−1.13	-0.35 ± 0.04	−0.35	0.24	0.65	1.66×10^{-4}	0.00	
CD-33 3337	5979	3.86	−1.36	-0.61 ± 0.04	−0.62	0.28	0.69	1.50×10^{-4}	0.01	
CD-43 6810	5945	4.26	−0.43	-0.12 ± 0.04	−0.12	0.17	0.65	6.80×10^{-1}	0.00	
CD-45 3283	5597	4.55	−0.91	-0.46 ± 0.03	−0.46	0.23	0.66	1.50×10^{-4}	0.00	
CD-51 4628	6153	4.31	−1.30	-0.80 ± 0.03	−0.79	0.31	0.69	1.50×10^{-4}	0.01	
CD-57 1633	5873	4.28	−0.90	-0.47 ± 0.03	−0.47	0.23	0.68	1.50×10^{-4}	0.00	
CD-61 282	5759	4.31	−1.23	-0.57 ± 0.05	−0.58	0.27	0.69	1.50×10^{-4}	0.01	
G 05-19	5854	4.26	−1.18	-0.61 ± 0.04	−0.62	0.28	0.69	1.50×10^{-4}	0.01	
G 05-40	5795	4.17	−0.81	-0.12 ± 0.03	−0.12	0.17	0.65	6.80×10^{-1}	0.00	
G 112-43	6074	4.03	−1.25	-0.73 ± 0.04	−0.74	0.30	0.69	1.50×10^{-4}	0.01	
G 119-64	6181	4.18	−1.48	-0.88 ± 0.05	−0.89	0.32	0.67	1.50×10^{-4}	0.01	
G 150-40	5968	4.09	−0.81	-0.49 ± 0.05	−0.49	0.24	0.69	1.50×10^{-4}	0.00	
G 15-23	5297	4.57	−1.10	-0.39 ± 0.05	−0.40	0.11	0.65	1.50×10^{-4}	0.01	
G 159-50	5624	4.37	−0.93	-0.35 ± 0.04	−0.35	0.24	0.65	1.66×10^{-4}	0.00	
G 170-56	5994	4.12	−0.92	-0.47 ± 0.04	−0.47	0.23	0.68	1.50×10^{-4}	0.00	
G 176-53	5523	4.48	−1.34	-0.72 ± 0.05	−0.74	0.30	0.69	1.50×10^{-4}	0.02	
G 180-24	6004	4.21	−1.39	-0.65 ± 0.04	−0.64	0.28	0.66	1.50×10^{-4}	0.01	
G 18-28	5372	4.41	−0.83	-0.20 ± 0.04	−0.20	0.25	0.65	6.50×10^{-1}	0.00	
G 18-39	6040	4.21	−1.39	-0.71 ± 0.04	−0.70	0.29	0.65	1.50×10^{-4}	0.01	
G 188-22	5974	4.18	−1.32	-0.52 ± 0.03	−0.52	0.25	0.68	1.50×10^{-4}	0.00	
G 20-15	6050	4.34	−1.45	-0.91 ± 0.06	−0.91	0.33	0.69	1.50×10^{-4}	0.00	
G 24-13	5673	4.32	−0.72	$+0.02 \pm 0.04$	−0.20	0.25	0.65	6.50×10^{-1}	0.22	
G 31-55	5638	4.30	−1.10	-0.42 ± 0.04	−0.42	0.16	0.68	1.50×10^{-4}	0.00	
G 53-41	5859	4.27	−1.20	-0.90 ± 0.05	−0.90	0.32	0.65	1.50×10^{-4}	0.00	
G 5-36	6013	4.23	−1.23	-0.51 ± 0.04	−0.51	0.25	0.65	1.50×10^{-4}	0.00	
G 56-36	5933	4.28	−0.94	-0.35 ± 0.03	−0.35	0.24	0.65	1.66×10^{-4}	0.00	
G 66-22	5236	4.41	−0.86	-0.47 ± 0.09	−0.47	0.23	0.69	1.50×10^{-4}	0.00	
G 75-31	6010	4.02	−1.03	-0.58 ± 0.04	−0.59	0.27	0.65	1.50×10^{-4}	0.01	
G 82-05	5277	4.45	−0.75	-0.41 ± 0.04	−0.41	0.11	0.67	1.50×10^{-4}	0.00	
G 85-13	5628	4.38	−0.59	-0.05 ± 0.04	−0.20	0.25	0.65	6.50×10^{-4}	0.15	
G 99-21	5487	4.39	−0.67	-0.08 ± 0.04	−0.20	0.25	0.65	6.50×10^{-1}	0.12	
HD 106516	6196	4.42	−0.68	-0.01 ± 0.04	−0.20	0.25	0.65	6.50×10^{-4}	0.19	
HD 103723	5938	4.19	−0.80	-0.38 ± 0.03	−0.38	0.25	0.65	1.54×10^{-4}	0.00	
HD 105004	5754	4.30	−0.82	-0.42 ± 0.03	−0.42	0.16	0.68	1.50×10^{-4}	0.00	
HD 160693	5714	4.27	−0.49	0.02 ± 0.05	−0.20	0.25	0.65	6.50×10^{-4}	0.18	
HD 113679	5672	3.99	−0.81	-0.08 ± 0.04	−0.20	0.25	0.65	6.50×10^{-4}	0.12	
HD 111980	5778	3.96	−1.08	-0.31 ± 0.04	−0.31	0.20	0.68	1.92×10^{-4}	0.00	
HD 114762 A	5856	4.21	−0.70	-0.14 ± 0.03	−0.14	0.21	0.65	6.80×10^{-1}	0.00	
HD 120559	5412	4.50	−0.89	-0.32 ± 0.04	−0.32	0.22	0.67	1.83×10^{-4}	0.00	
HD 121004	5669	4.37	−0.70	-0.14 ± 0.04	−0.14	0.21	0.65	6.80×10^{-1}	0.00	
HD 126681	5507	4.45	−1.17	-0.46 ± 0.05	−0.46	0.23	0.66	1.50×10^{-4}	0.00	
HD 132475	5646	3.76	−1.49	-0.64 ± 0.04	−0.64	0.28	0.66	1.50×10^{-4}	0.00	
HD 148816	5832	4.14	−0.71	-0.12 ± 0.05	−0.12	0.17	0.65	6.80×10^{-1}	0.00	
HD 159482	5737	4.31	−0.73	-0.09 ± 0.03	−0.10	0.11	0.65	6.50×10^{-1}	0.01	
HD 163810	5501	4.56	−1.20	-0.67 ± 0.06	−0.67	0.29	0.69	1.50×10^{-4}	0.00	
HD 175179	5713	4.33	−0.65	0.01 ± 0.09	−0.20	0.25	0.65	6.50×10^{-4}	0.21	
HD 17820	5773	4.22	−0.67	-0.05 ± 0.05	−0.20	0.25	0.65	6.50×10^{-4}	0.15	
HD 179626	5853	4.16	−1.02	-0.31 ± 0.03	−0.31	0.20	0.68	1.92×10^{-4}	0.00	
HD 189558	5620	3.81	−1.12	-0.35 ± 0.05	−0.35	0.24	0.65	1.66×10^{-4}	0.00	
HD 193901	5663	4.39	−1.08	-0.57 ± 0.03	−0.58	0.27	0.69	1.50×10^{-4}	0.01	
HD 194598	5934	4.33	−1.08	-0.56 ± 0.03	−0.58	0.27	0.69	1.50×10^{-4}	0.02	
HD 199289	5810	4.28	−1.04	-0.35 ± 0.03	−0.35	0.24	0.65	1.66×10^{-4}	0.00	
HD 205650	5698	4.32	−1.17	-0.45 ± 0.04	−0.45	0.22	0.67	1.50×10^{-4}	0.00	
HD 219617	5862	4.28	−1.45	-0.77 ± 0.05	−0.77	0.30	0.66	1.50×10^{-4}	0.00	
HD 222766	5334	4.27	−0.67	-0.03 ± 0.06	−0.20	0.25	0.65	6.50×10^{-4}	0.17	
HD 22879	5759	4.25	−0.85	-0.15 ± 0.03	−0.15	0.23	0.65	6.50×10^{-1}	0.00	
HD 230409	5318	4.54	−0.85	-0.29 ± 0.05	−0.29	0.17	0.67	1.97×10^{-4}	0.00	
HD 233511	6006	4.23	−1.55	-0.85 ± 0.06	−0.85	0.32	0.69	1.50×10^{-4}	0.00	
HD 241253	5831	4.31	−1.10	-0.36 ± 0.07	−0.36	0.24	0.67	1.68×10^{-4}	0.00	
HD 250792 A	5489	4.47	−1.01	-0.49 ± 0.03	−0.49	0.24	0.69	1.50×10^{-4}	0.00	
HD 25704	5868	4.26	−0.85	-0.26 ± 0.07	−0.26	0.27	0.65	6.90×10^{-1}	0.00	
HD 284248	6135	4.25	−1.57	-0.98 ± 0.04	−0.98	0.34	0.69	1.50×10^{-4}	0.00	
HD 3567	6051	4.02	−1.16	-0.66 ± 0.03	−0.67	0.29	0.69	1.50×10^{-4}	0.01	
HD 51754	5767	4.29	−0.58	-0.05 ± 0.06	−0.20	0.25	0.65	6.50×10^{-4}	0.17	
HD 59392	6012	3.91	−1.60	-0.96 ± 0.05	−0.96	0.33	0.66	1.50×10^{-4}	0.00	
HD 76932	5877	4.13	−0.87	-0.22 ± 0.03	−0.21	0.25	0.65	6.80×10^{-1}	0.01	
HD 97320	6008	4.19	−1.17	-0.48 ± 0.05	−0.48	0.24	0.66	1.50×10^{-4}	0.00	
Average					-0.44					
MAD										0.19

^{a} [61]; ^{o} This Work

4.2. Statistical Analysis and Comparison with Observations

To evaluate the consistency between our model predictions, denoted as $[O/H]^o$, and observational determinations from the literature, $[O/H]^a$, we carried out a quantitative statistical analysis. For the full sample of 57 stars, a Pearson correlation test yields a correlation coefficient of $r = 0.98$, indicative of a strong and highly significant positive linear relationship. This result demonstrates that the model reproduces the observed oxygen abundance trends with remarkable fidelity.

The mean absolute deviation (MAD) of the observed $[O/H]$ values within each cluster is approximately 0.019 dex, underscoring both the internal consistency of the data and the robustness of our computational framework. These results collectively validate the reliability of the adopted reaction network, reinforcing the hypothesis that the NOFNe cycle, operating under the specified stellar conditions and coupled with a rotational ejection mechanism, provides a viable explanation for the oxygen abundance patterns observed in these systems.

A comparison between computed and observed ^{16}O abundances is presented in Table 5, drawing observational data from Ramírez *et al.* (2012) [61]. Figure 6 further illustrates this comparison, displaying the abundances as a function of [Fe/H]. Error bars on the calculated values (open circles) represent uncertainties propagated from differences in adopted reaction rates, specifically between the NACRE II and Iliadis et al. (2010) [48] compilations.

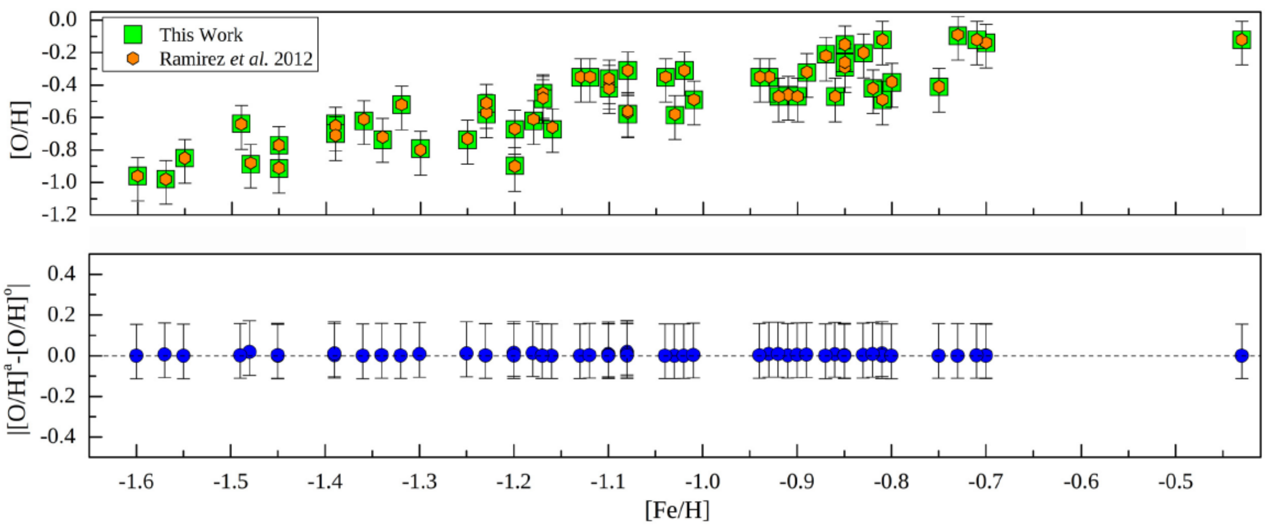

Figure 6. *A comparative view of calculated and observed values of abundances of those selected stars of Table 5 is shown. The open boxes are the values obtained from the literature [61], and the open circles are the values calculated from this work.*

5. Discussion & Conclusion

In this study, we have carried out a comprehensive theoretical investigation of oxygen abundances in 67 metal-poor field halo and disk stars using a local thermodynamic equilibrium (LTE) framework to model the NOFNe nuclear reaction cycle under conditions representative of advanced stellar burning phases. Our calculations, performed over a temperature range of 1×10^8 ˘ 3.5×10^8 K and a density of 10^2 g cm^{-3}, employed the 777 nm O I triplet lines to derive LTE oxygen abundances ($[O/H]_{LTE}$). The results exhibit close agreement with empirical values reported in the literature, thereby validating the applicability of the NOFNe framework in reproducing observed stellar oxygen trends. These findings underscore the significance of proton-capture pathways within the NOFNe cycle, particularly when coupled with rotational effects and mass loss, in resolving long-standing discrepancies in nucleosynthetic yields. Collectively, this work highlights the role of the NOFNe pathway¯linking nitrogen, oxygen, fluorine, and neon¯as a crucial mechanism for oxygen synthesis in helium-enriched stellar environments, offering important implications for models of Galactic chemical evolution.

The mean [O/H] value for the entire sample is ˘ 0.49 dex, with a mean absolute deviation (MAD) of 0.19 dex. This scatter lies within the typical observational uncertainties of high-resolution spectroscopic studies of metal-poor stars (∼0.15˝0.20 dex), thereby confirming the reliability of our abundance predictions. Complementing this, the Pearson correlation coefficient of $r = 0.98$ between our computed abundances and observed literature values demonstrates an exceptionally strong linear agreement, underscoring the model's ability to reproduce both the central trend and the intrinsic dispersion in oxygen abundances. Taken together, the MAD and correlation statistics provide dual validation of the computational framework, highlighting its robustness across a broad sample of stellar populations. This statistical consistency strengthens the case for the adopted approach, which employs enhanced model atmospheres and refined abundance computation methods sensitive to parameters such as hydrogen ($X_{\rm H}$) and oxygen ($X_{\rm O}$) mass fractions. By incorporating proton-capture pathways within the NOFNe cycle and accounting for rotational mass loss, the model successfully resolves long-standing discrepancies in nucleosynthetic yield predictions [37, 58, 59]. In particular, the NOFNe pathway¯coupling nitrogen, oxygen, fluorine, and neon¯emerges as a principal mechanism for oxygen synthesis in helium-enriched environments typical of late stellar evolutionary stages [11, 35].

Our findings strengthen the evidence for distinct chemical signatures among thick-disk, high-α halo, and low-α halo stars, thereby providing critical constraints for Galactic Chemical Evolution (GCE) models. The observed oxygen enhancements are consistent with enrichment dominated by massive stars through core-collapse supernovae (Type II SNe), preceding the delayed contribution from Type Ia SNe [16, 17]. This persistent α-enhancement underscores the interpretation of these stars as relics of the Milky Way's early assembly, with oxygen serving as a reliable tracer of burst-like star formation episodes [14, 15]. At the same time, the subtle $[{\rm O}/{\rm H}]$ variations among subpopulations point to the role of halo accretion processes, wherein gas from satellite galaxies modifies local abundance patterns [4, 5]. Finally, the incorporation of rotational effects in massive stars offers a consistent explanation for observed anomalies, as rotation-driven mixing and mass loss enhance the ejection of processed material into the interstellar medium, influencing subsequent stellar generations [11, 36]. Collectively, these results confirm that the combined action of core-collapse supernovae, accretion processes, and stellar rotation governs the oxygen abundance trends observed in halo and thick-disk stars.

Comparisons with observational data, particularly those of Ramírez et al. (2012) [61], demonstrate that our computed abundances are in close agreement with high-resolution spectroscopic measurements, with residual uncertainties primarily attributable to nuclear reaction rate variations (e.g., NACRE II [50]; Iliadis et al. 2010 [48]). For example, in the subset of stars presented in Table 5 (e.g., HD 106516, HD 113679), the calculated $[{\rm O}/{\rm H}]$ values deviate by no more than 0.02 dex, confirming the robustness and precision of the model. These results reinforce the central role of α-capture reactions in regulating oxygen abundances, while also emphasizing the necessity of incorporating non-standard mixing and mass-loss processes into stellar evolution models [34, 40, 41]. The minor discrepancies observed can likely be attributed to observational limitations such as non-LTE effects or line blending, as well as theoretical uncertainties in convection modeling [36]. Taken together, the strong agreement between predicted and observed abundances lends further confidence to the NOFNe framework as a viable explanation for the oxygen trends across different stellar populations.

The implications of this work extend beyond individual stellar populations to broader astrophysical contexts. By refining the role of proton-capture pathways in the NOFNe cycle and incorporating rotational dynamics, we provide new insights into oxygen nucleosynthesis that are essential for accurate Galactic Chemical Evolution (GCE) models and for interpreting large-scale survey data from missions such as Gaia and APOGEE [3, 4]. Oxygen, as the third most abundant element and a key α-element, serves as a cornerstone for probing stellar interiors, galactic enrichment, and cosmological evolution [19, 20]. Our results suggest that these processes help resolve abundance puzzles in metal-poor environments, particularly in globular clusters exhibiting multiple populations [11]. Subtle deviations in [O/H] among stellar subpopulations may reflect accretion events in the Galactic halo, where infalling gas from satellite galaxies alters chemical signatures, while rotational mixing and ejection in massive stars distribute processed material into the interstellar medium, shaping subsequent stellar generations. Looking forward, multidimensional hydrodynamic simulations that capture convective mixing and rotational instabilities will be critical for improving yield predictions, while updated low-energy reaction rates from facilities such as LUNA can enhance precision at astrophysically relevant temperatures. Finally, expanding observational efforts to larger samples of halo and disk stars with next-generation telescopes will provide stringent tests of the NOFNe framework, offering deeper insight into the Milky Way's accretion history and chemical evolution.

ORCID

0009-0005-4510-7519 (Swapnajyoti Sarma)
0000-0002-8154-2009 (Mrinmay Medhi)
0009-0006-2712-4996 (Apurba Talukdar)
0009-0004-9032-8145 (Jinturaj Talukdar)
0000-0002-2163-3734 (Devapratim Mahanta)
0009-0003-1952-2124 (Dhanjit Talukdar)
0000-0003-0490-2637 (Upakul Mahanta)
0009-0007-2446-5469 (Arup Bharali)

Abbreviations

AGB	Asymptotic Giant Branch
CNOF	Carbon-Nitrogen-Oxygen-Fluorine
ISM	Interstellar Medium
LUNA	Laboratory for Underground Nuclear Astrophysics
MAD	Mean Absolute Deviation
RGB	Red Giant Branch

Author Contributions

Swapnajyoti Sarma: Conceptualization, Methodology, Formal analysis, Investigation, Writing – original draft.

Mrinmay Medhi: Data curation, Software, Validation, Visualization, Writing – original draft, Writing – review &

editing.

Apurba Talukdar: Methodology, Formal analysis, Investigation, Validation.

Jinturaj Talukdar: Data curation, Resources, Software, Visualization.

Devapratim Mahanta: Investigation, Formal analysis, Validation.

Dhanjit Talukdar: Supervision, Project administration, Resources.

Upakul Mahanta: Supervision, Methodology, Writing – review & editing.

Arup Bharali: Supervision, Funding acquisition, Writing – review & editing.

Conflicts of Interest

The authors declare no conflicts of interest.

References

[1] A. G. Bruzual,Star clusters as simple stellar populations, Philos. Trans. R. Soc. A 368, 783–799 (2010), https://doi.org/10.1098/rsta.2009.0258

[2] W. E. Harris, Globular cluster systems in galaxies beyond the Local Group, Annu. Rev. Astron. Astrophys. 29, 543–579 (1991), https://doi.org/10.1146/annurev.aa.29.090191.002551

[3] E. Carretta, A. Bragaglia, R. G. Gratton, S. Lucatello, G. Catanzaro, F. Leone, M. Bellazzini, R. Claudi, V. D'Orazi, Y. Momany et al., Na-O anticorrelation and HB: VII. The chemical composition of first and second-generation stars in 15 globular clusters from GIRAFFE spectra, Astron. Astrophys. 505, 117–138 (2009), https://doi.org/10.1051/0004-6361/200912096

[4] R. G. Gratton, E. Carretta, and A. Bragaglia, Multiple populations in globular clusters: Lessons learned from the Milky Way globular clusters, Astron. Astrophys. Rev. 20, 50 (2012), https://doi.org/10.1007/s00159-012-0050-3

[5] S. Villanova, D. Geisler, R. G. Gratton, and S. Cassisi, The metallicity spread and the age–metallicity relation of ω Centauri, Astrophys. J. 791, 107 (2014), https://doi.org/10.1088/0004-637X/791/2/107

[6] G. Busso, S. Cassisi, G. Piotto, M. Castellani, M. Romaniello, M. Catelan, S. G. Djorgovski, A. Recio-Blanco, A. Renzini, et al. The peculiar horizontal branch morphology of the Galactic globular clusters NGC 6388 and NGC 6441: new insights from UV observations, Astron. Astrophys. 474, 105–119 (2007), https://doi.org/10.1051/0004-6361:20077806

[7] S. Villanova, G. Piotto, A. F. Marino, A. P. Milone, A. Bellini, L. R. Bedin, Y. Momany, and A. Renzini, The multipopulation phenomenon in Galactic globular clusters: M4 and M22, Proc. Int. Astron. Union 5, 326–332 (2009), https://doi.org/10.1017/S1743921309991219

[8] N. Bastian and C. Lardo, Multiple stellar populations in globular clusters, Annu. Rev. Astron. Astrophys. 56, 83–136 (2018), https://doi.org/10.1146/annurev-astro-081817-051839

[9] R. Gratton, A. Bragaglia, E. Carretta, V. D'Orazi, S. Lucatello, and A. Sollima, What is a globular cluster? An observational perspective, Astron. Astrophys. Rev. 27, 8 (2019), https://doi.org/10.1007/s00159-019-0119-3

[10] C. Lardo, M. Salaris, S. Cassisi, and N. Bastian, Confirmation of a metallicity spread amongst first population stars in globular clusters, Astron. Astrophys. 662, A117 (2022), https://doi.org/10.1051/0004-6361/202243843

[11] T. Decressin, G. Meynet, C. Charbonnel, N. Prantzos, and S. Ekström, Fast rotating massive stars and the origin of the abundance patterns in galactic globular clusters, Astron. Astrophys. 464, 1029–1044 (2007), https://doi.org/10.1051/0004-6361:20066013

[12] P. A. Denissenkov, D. A. VandenBerg, F. D. A. Hartwick, F. Herwig, A. Weiss, and B. Paxton, The primordial and evolutionary abundance variations in globular-cluster stars: a problem with two unknowns, Mon. Not. R. Astron. Soc. 448, 3314–3324 (2015), https://doi.org/10.1093/mnras/stv211

[13] A. Kuruvanthodi, D. Schaerer, M. Messa, A. Adamo, C. Usher, C. Charbonnel, and R. Marques-Chaves, Search strategies for supermassive stars in young clusters and application to nearby galaxies, Astron. Astrophys. 674, A140 (2023), https://doi.org/10.1051/0004-6361/202245695

[14] K. Nomoto, C. Kobayashi, and N. Tominaga, Nucleosynthesis in stars and the chemical enrichment of galaxies, Annu. Rev. Astron. Astrophys. 51, 457–509 (2013), https://doi.org/10.1146/annurev-astro-082812-140956

[15] F. Matteucci, Chemical evolution of galaxies, Astronomy and Astrophysics Library, Springer, Berlin (2012), https://doi.org/10.1007/978-3-642-22491-1

[16] B. M. Tinsley, Evolution of the stars and gas in galaxies, Astrophys. J. 151, 547 (1968), https://doi.org/10.1086/149455

[17] T. Nakamura, H. Umeda, K. Nomoto, F.-K. Thielemann, and A. Burrows, Nucleosynthesis in Type II supernovae and the abundances in metal-poor stars, Astrophys. J. 517, 193–208 (1999), https://doi.org/10.1086/307167

[18] R. Gratton, C. Sneden, and E. Carretta, Abundance variations within globular clusters, Annu. Rev. Astron. Astrophys. 42, 385–440 (2004), https://doi.org/10.1146/annurev.astro.42.053102.133945

[19] B. S. Meyer, L. R. Nittler, A. N. Nguyen, and S. Messenger, Nucleosynthesis and chemical evolution of oxygen, Rev. Mineral. Geochem. 68, 31–53 (2008), https://doi.org/10.2138/rmg.2008.68.4

[20] M. Asplund, N. Grevesse, A. J. Sauval, and P. Scott, The chemical composition of the Sun, Annu. Rev. Astron. Astrophys. 47, 481–522 (2009), https://doi.org/10.1146/annurev.astro.46.060407.145222

[21] C. Sneden, R. P. Kraft, C. F. Prosser, and G. E. Langer, Oxygen abundances in halo giants. III - Giants in the mildly metal-poor globular cluster M5, Astron. J. 104, 2121 (1992), https://doi.org/10.1086/116388

[22] D. Yong, B. W. Carney, and M. L. T. de Almeida, Elemental abundance ratios in stars of the outer Galactic disk. I. Open clusters, Astron. J. 130, 597–625 (2005), https://doi.org/10.1086/430934

[23] A. Savino, D. Massari, A. Bragaglia, E. Dalessandro, and E. Tolstoy, M13 multiple stellar populations seen with the eyes of Strömgren photometry, Mon. Not. R. Astron. Soc. 474, 4438–4446 (2017), https://doi.org/10.1093/mnras/stx3093

[24] P. Ventura and P. Marigo, Asymptotic giant branch stars at low metallicity: the challenging interplay between the mass-loss and molecular opacities: Mass-loss and opacities in AGB modelling, Mon. Not. R. Astron. Soc. 408, 2476–2486 (2010), https://doi.org/10.1111/j.1365-2966.2010.17304.x

[25] G. Fragione and F. Antonini, Massive binary star mergers in galactic nuclei: implications for blue stragglers, binary S-stars, and gravitational waves, Mon. Not. R. Astron. Soc. 488, 728–738 (2019), https://doi.org/10.1093/mnras/stz1723

[26] C. Lardo, E. Pancino, M. Bellazzini, A. Bragaglia, P. Donati, G. Gilmore, S. Randich, S. Feltzing, R. D. Jeffries, A. Vallenari, et al. The Gaia-ESO Survey: Kinematics of seven Galactic globular clusters, Astron. Astrophys. 573, A115 (2015), https://doi.org/10.1051/0004-6361/201425036

[27] G. C. Myeong, N. W. Evans, V. Belokurov, J. L. Sanders, and S. E. Koposov, The Sausage Globular Clusters, Astrophys. J. Lett. 863, L28 (2018), https://doi.org/10.3847/2041-8213/aad7f7

[28] G. Tautvaišienė, B. Edvardsson, E. Puzeras, and I. Ilyin, Chemical composition of evolved stars in the open cluster NGC 7789, Astron. Astrophys. 431, 933–942 (2005), https://doi.org/10.1051/0004-6361:20041935

[29] S. Cassisi, M. Salaris, and G. Bono, The shape of the red giant branch bump as a diagnostic of partial mixing processes in low-mass stars, Astrophys. J. 565, 1231–1238 (2002), https://doi.org/10.1086/324695

[30] G. Carraro, D. Geisler, S. Villanova, P. M. Frinchaboy, and S. R. Majewski, Old open clusters in the outer Galactic disk, Astron. Astrophys. 476, 217–227 (2007), https://doi.org/10.1051/0004-6361:20078113

[31] G. Tautvaišienė, A. Drazdauskas, A. Bragaglia, S. Randich, and R. Ženovienė, CNO abundances and carbon isotope ratios in evolved stars of the open clusters NGC 2324, NGC 2477, and NGC 3960, Astron. Astrophys. 595, A16 (2016), https://doi.org/10.1051/0004-6361/201629273

[32] L. Magrini, S. Randich, G. Kordopatis, N. Prantzos, D. Romano, V. Adibekyan, M. Bergemann, K. Cunha, P. de Laverny, A. Recio-Blanco, Š. Mikolaitis, F. Matteucci, V. Silva Aguirre, and O. Snaith, Open clusters towards the Galactic centre: chemistry and dynamics, Astron. Astrophys., 523, A11, 2010. http://dx.doi.org/10.1051/0004-6361/201015395

[33] A. B. S. Reddy, D. L. Lambert, and G. Gonzalez, Comprehensive abundance analysis of red giants in the anticentre open clusters NGC 6791, NGC 6819, NGC 7789, Mon. Not. R. Astron. Soc., 431, 3338–3351, 2013. http://dx.doi.org/10.1093/mnras/stt412

[34] M. Salaris, S. Cassisi, A. Weiss, Red Giant Branch Stars: Theoretical Framework, Publications of the Astronomical Society of the Pacific, 114, 375–402, 2002. https://doi.org/10.1086/342498

[35] T. Rauscher, A. Heger, R. D. Hoffman, and S. E. Woosley, Nucleosynthesis in massive stars with improved nuclear and stellar physics, Astrophys. J. 576, 323–348 (2002), https://doi.org/10.1086/341728

[36] M. Salaris and S. Cassisi, Chemical element transport in stellar evolution models, R. Soc. Open Sci. 4, 170192 (2017), https://doi.org/10.1098/rsos.170192

[37] U. Mahanta, A. Goswami, H. Duorah, and K. Duorah, p-capture reaction cycles in rotating massive stars and their impact on elemental abundances in globular cluster stars: A case study of O, Na and Al, Res. Astron. Astrophys. 17, 080 (2017), https://doi.org/10.1088/1674-4527/17/8/80

[38] F. Käppeler, R. Gallino, S. Bisterzo, and W. Aoki, The s process: Nuclear physics, stellar models, and observations, Rev. Mod. Phys. 83, 157–193 (2011), https://doi.org/10.1103/revmodphys.83.157

[39] C. Iliadis, Nuclear physics of stars, Wiley, (2007), https://doi.org/10.1002/9783527618750

[40] M. Salaris and S. Cassisi, Evolution of stars and stellar populations, Wiley, (2005), https://doi.org/10.1002/0470033452

[41] P. A. Denissenkov and C. A. Tout, On a physical mechanism for extra mixing in globular cluster red giants, Mon. Not. R. Astron. Soc. 316, 395–406 (2000), https://doi.org/10.1046/j.1365-8711.2000.03498.x

[42] J.-W. Lee and B. W. Carney, Chemical abundances of three metal-poor globular clusters (NGC 6287, NGC 6293, and NGC 6541) in the inner halo, Astron. J. 124, 1511–1527 (2002), https://doi.org/10.1086/341948

[43] S. Cristallo, O. Straniero, L. Piersanti, and D. Gobrecht, Evolution, nucleosynthesis, and yields of AGB stars at different metallicities. III. Intermediate-mass models, revised low-mass models, and the pH-FRUITY interface, Astrophys. J. Suppl. Ser. 219, 40 (2015), https://doi.org/10.1088/0067-0049/219/2/40

[44] S. A. Heap, R. J. Stancliffe, J. C. Lattanzio, and D. S. P. Dearborn, Three-dimensional modelling of proton ingestion episodes in low-mass stars, AIP Conf. Proc., 367–369 (2012), https://doi.org/10.1063/1.4754389

[45] N. Mowlavi, A. Jorissen, and M. Arnould, Fluorine production in asymptotic giant branch stars, Symp. Int. Astron. Union 177, 459–462 (2000), https://doi.org/10.1017/s0074180900002734

[46] K. Lodders, Solar system abundances and condensation temperatures of the elements, Astrophys. J. 591, 1220–1247 (2003), https://doi.org/10.1086/375492

[47] A. Best, S. Falahat, J. Görres, M. Couder, R. deBoer, A. Kontos, K.-L. Kratz, P. J. LeBlanc, Q. Li, S. O'Brien, K. Sonnabend, R. Talwar, E. Uberseder, and M. Wiescher, Low-energy resonances in the ^{14}N(α,γ)^{18}F reaction, Phys. Rev. C 87, 045805 (2013), https://doi.org/10.1103/PhysRevC.87.045805

[48] C. Iliadis, R. Longland, A. E. Champagne, A. Coc, and R. Fitzgerald, Charged-particle thermonuclear reaction rates: II. Tables and graphs of reaction rates and probability density functions, Nucl. Phys. A 841, 31–250 (2010), https://doi.org/10.1016/j.nuclphysa.2010.04.009

[49] C. G. Bruno, M. Aliotta, P. Descouvemont, A. Best, T. Davinson, D. Bemmerer, A. Boeltzig, C. Broggini, A. Caciolli, F. Cavanna, et al., Improved astrophysical rate for the ^{18}O(p,α)^{15}N reaction by underground measurements, Phys. Lett. B 790, 237–242 (2019), https://doi.org/10.1016/j.physletb.2019.01.017

[50] Y. Xu, K. Takahashi, S. Goriely, M. Arnould, M. Ohta, and H. Utsunomiya, NACRE II: An update of the NACRE compilation of charged-particle-induced thermonuclear reaction rates for nuclei with mass number $A < 16$, Nucl. Phys. A 918, 61–169 (2013), https://doi.org/10.1016/j.nuclphysa.2013.09.007

[51] R. Fang, J. Görres, R. J. deBoer, S. Moylan, A. T. Sanchez, T. L. Bailey, S. Carmichael, J. Koros, K. Lee, K. Manukyan, et al., Energy, strength, and α width measurements of $E_{\text{c.m.}} = 1323$ and 1487 keV resonances in ^{15}N(α,γ)^{19}F, Phys. Rev. C 110, 025806 (2024), https://doi.org/10.1103/physrevc.110.025806

[52] L. Y. Zhang, J. J. He, A. Parikh, S. W. Xu, H. Yamaguchi, D. Kahl, S. Kubono, P. Mohr, J. Hu, P. Ma, et al., Thermonuclear ^{19}F(p,α)^{16}O reaction rate revised and astrophysical implications, Astrophys. J. 913, 44 (2021), https://doi.org/10.3847/1538-4357/abf1e7

[53] D. R. Tilley, H. R. Weller, and C. M. Cheves, Energy levels of light nuclei A = 16-17, Nucl. Phys. A 564, 1–183 (1993), https://doi.org/10.1016/0375-9474(93)90073-7

[54] J. Frost-Schenk, P. Adsley, A. M. Laird, R. Longland, C. Angus, C. Barton, A. Choplin, C. Aa. Diget, R. Hirschi, C. Marshall, et al., The impact of ^{17}O + α reaction rate uncertainties on the s-process in rotating massive stars, Mon. Not. R. Astron. Soc. 514, 2650–2657 (2022), https://doi.org/10.1093/mnras/stac1373

[55] P. Mohr, Low-energy direct capture in the ^{16}O(α,γ)^{20}Ne reaction, Phys. Rev. C 72, 035803 (2005), https://doi.org/10.1103/physrevc.72.035803

[56] C. Angulo, M. Arnould, M. Rayet, P. Descouvemont, D. Baye, C. Leclercq-Willain, A. Coc, S. Barhoumi, P. Aguer, et al., A compilation of charged-particle induced thermonuclear reaction rates, Nucl. Phys. A 656, 3–183 (1999), https://doi.org/10.1016/s0375-9474(99)00030-5

[57] M. La Cognata, C. Spitaleri, and A. M. Mukhamedzhanov, Effect of high-energy resonances on the ^{18}O(p,α)^{15}N reaction rate at AGB and post-AGB relevant temperatures, Astrophys. J. 723, 1512–1522 (2010), https://doi.org/10.1088/0004-637x/723/2/1512

[58] M. Medhi, D. P. Mahanta, and U. Mahanta, Contribution of proton capture reactions to the abundances of phosphorus and sulfur in FGK stars, J. Astrophys. Astron. 44, 1 (2023), https://doi.org/10.1007/s12036-023-09913-3

[59] A. Talukdar, A. Rajbongshi, M. Medhi, and U. Mahanta, Impact of Proton-Capture Reaction Cycles on Isotopic Oxygen (^{16}O) Abundances in Stars from Galactic Open Clusters NGC 2324, NGC 2477, and NGC 3960, Am. J. Astron. Astrophys., 12, 112–125, 2025. https://doi.org/10.11648/j.ajaa.20251203.16

[60] D. D. Clayton, Principles of Stellar Evolution and Nucleosynthesis, Univ. Chicago Press, Chicago, 1983.

[61] I. Ramírez, J. Meléndez, and J. Chanamé, Oxygen abundances in low- and high-α field halo stars and the discovery of two field stars born in globular clusters, Astrophys. J. 757, 164 (2012), https://doi.org/10.1088/0004-637x/757/2/164